Nanoscale

ROYAL SOCIETY OF CHEMISTRY

PAPER

View Article Online
View Journal | View Issue

Cite this: *Nanoscale*, 2025, **17**, 230

Preceramic polymer-hybridized phenolic aerogels and the derived ZrC/SiC/C ceramic aerogels with ultrafine nanocrystallines

Ding Nie,†[a] Hangyu Zhong,†[a] Hongli Hu,[a] Zhenhua Luo*[c] and Bo-xing Zhang *[a,b]

Phenolic and carbon aerogels have important applications for thermal insulation and ablative resistance materials in aerospace field. However, their antioxidant ability in long-term high-temperature aerobic environments faces serious challenges. To solve this problem, Zr/Si preceramic polymer hybridized phenolic resin (PR-ZS) aerogels were prepared *via* a facile sol–gel method. Compared with pure phenolic aerogel, the hybrid aerogels possess similar porous microstructure but larger specific surface area, better thermo-oxidative stability, and higher compressive strength. After carbonization at 1700 °C, the hybrid aerogels can be transformed to carbide ceramic aerogels with ultrafine nanocrystalline ZrC and SiC particles embedded in the carbon matrix. Ceramic aerogels exhibit good thermal insulative and anti-ablative properties in a butane torch simulated high-temperature and aerobic environment. The linear ablation rate is as low as 0.017 mm min^{-1}, and the backside temperature is below 330 °C at a 20 mm in-depth position after 300 s of burning test, when the front temperature is approximately 960 °C. This work provides a facile approach to fabricate hybrid phenolic aerogels and derived ZrC/SiC/C ceramic aerogels, which target on applications for extreme environments in aerospace field.

Received 24th August 2024,
Accepted 6th November 2024

DOI: 10.1039/d4nr03470h

rsc.li/nanoscale

[a]*South China Advanced Institute for Soft Matter Science and Technology, School of Emergent Soft Matter, South China University of Technology, Guangzhou 510640, China. E-mail: bxzhang@scut.edu.cn*
[b]*Guangdong Provincial Key Laboratory of Functional and Intelligent Hybrid Materials and Devices, South China University of Technology, Guangzhou 510640, China*
[c]*Key Laboratory of Science and Technology on High-tech Polymer Materials, Institute of Chemistry, Chinese Academy of Sciences, Beijing, P. R. China. E-mail: z.h.luo@iccas.ac.cn*
† Ding Nie and Hangyu Zhong equally contributed to this work.

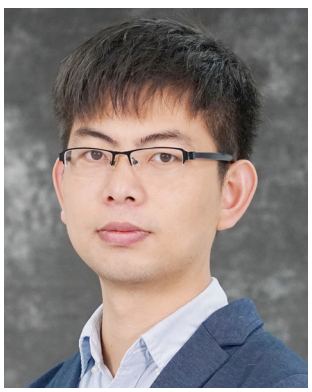

Bo-xing Zhang

Bo-xing Zhang received his PhD from the department of Applied Chemistry in Osaka University. In 2016, he joined the South China Advanced Institute for Soft Matter Science and Technology in South China University of Technology as a postdoctoral researcher. In 2019, he was promoted to an Associate Professor. Currently, his research interests focus on the fabrication and application of sol nanoparticles, ceramic microspheres, ceramic coatings, and organic–inorganic hybrid materials.

1. Introduction

Since aerogels were first developed by Kistler in 1931,[1] they have been widely used in various applications, such as thermal insulators,[2,3] catalyst supports,[4] absorbents,[5] electrodes for supercapacitors, *etc.*, owing to their low density, continuous porosity, large specific surface area, and extremely low thermal conductivity.[6–8] Phenolic resin (PR) has excellent properties, including flame retardancy, high char yield, good mechanical properties, and ablation resistance.[9–11] Phenolic aerogels derived from PR possess low density, low thermal conductivity, and excellent heat resistance, making them promising thermal protection and insulation materials in high temperature environments.[6,12]

At present, most PR aerogels are prepared using phenolic prepolymer as precursor with a sol–gel method, followed by ambient pressure drying. Jia *et al.*[13] and Xu *et al.*[14] conducted an interesting research on the fabrication of aerogels through the sol–gel reaction with resole-type PR, ethylene glycol (EG), water, and benzenesulfonyl chloride as starting materials. The porous morphology can be flexibly tuned by adjusting the composition of starting materials. However, PR aerogels encounter serious degradation and failure in long-term and high-temperature aerobic environments. Their poor mechanical properties caused by their inherent porous microstructure also limit their wide application.[15]

To solve these problems, two methods are commonly employed. One is to enhance PR aerogels by using fabrics with

low density and high porosity as 3D reinforcements.[16] The other is to introduce ceramic precursors, organic silicon, carbon nanotubes, or graphene oxide, *etc.*, into the porous skeleton of PR aerogels.[15,17–19] Huang *et al.*[20] developed a facile strategy to fabricate versatile phenolic aerogels by incorporating organic silicon into the molecular backbone of PR. The intriguing hierarchical microstructure afforded the aerogel composites multiple advantages, including high flexibility with a maximum cyclic compression strain of 70%, good thermal insulating performance, and remarkable hydrophobicity. Yin *et al.*[15] fabricated lightweight PR/silicon hybrid aerogels through a sol–gel reaction of PR, methyltrimethoxysilane (MTMS), and hexamethylenetetramine (HMTA) in EG solution. PR/silicon hybrid aerogels exhibited high thermal stability, low thermal conductivity, and good mechanical properties. Moreover, carbon-bonded carbon fiber matrix was used to fabricate enhanced aerogel composites which demonstrated good thermal insulation and ablative resistance performance under high-temperature oxyacetylene flame.

Carbon aerogels have received considerable attention in high-temperature insulation applications due to their excellent chemical stability and thermal stability in inert atmospheres.[21,22] Typically, carbon aerogels are prepared by high-temperature pyrolysis of organic aerogels.[23] Jia *et al.*[13] prepared lightweight and mechanically strong carbon aerogel monoliths (CAMs) based on PR aerogels which came from the sol–gel reaction of linear PR and HMTA. Yang *et al.*[24] prepared strong CAMs through polycondensation of resorcinol with formaldehyde by adding sodium carbonate and deionized water as catalyst and solvent, respectively. However, carbon aerogels burn rapidly when exposed to high-temperature aerobic atmospheres, which severely limits their practical application.[25] Generally, inorganic elements are incorporated into carbon materials to improve their oxidation resistance. Wu *et al.*[26] fabricated silica modified carbon aerogels (SCAs) *via* the sol–gel reaction of PR and siloxane, followed by ambient pressure drying and carbonization. During the carbonization process, amorphous SiO_2 particles gradually transform into crystalline SiC particles by carbothermal reduction reaction, which improves the oxidation resistance of SCAs. Liu *et al.*[27] fabricated carbon/modified halloysite nanotube (m-HNTs) composite aerogels with lower volumetric shrinkage (30.83%) and weight loss rate (26.76%) and higher compressive strength (4.43 MPa) by introducing m-HNTs into PR aerogels through chemical grafting, followed with carbonization treatment. Li *et al.*[28] prepared a novel TiB_2–B_4C/carbon (TB/C) aerogel composite by introducing TiB_2 and B_4C particles into phenolic aerogels through mechanical mixing and quick gelation. TiB_2 and B_4C particles reacted with the oxygen-containing molecules to form a TiO_2–B_2O_3 layer, which effectively improved the oxidation resistance and mechanical properties of phenolic aerogel composites. However, in the nanopowder route, dispersion of nanopowders is always a tough issue, and agglomeration of nanopowders in aerogels inevitably undermines the mechanical and thermal insulation performance.

In this work, we demonstrate a facile approach to prepare Zr/Si element hybridized phenolic (PR-ZS) aerogels and the derived ZrC/SiC/C ceramic aerogels with high mechanical strength and excellent thermal properties through the sol–gel reaction of PR, Zr/Si precursor, and HMTA, followed by ambient pressure drying and carbonization. The microstructure, thermo-oxidative stability, porous properties, thermal conductivity, and mechanical performance of the hybrid aerogels and ZrC/SiC/C ceramic aerogels with various contents of Zr/Si precursor were comprehensively investigated. In addition, the ablative resistance and thermal insulation properties of ZrC/SiC/C ceramic aerogels were evaluated.

2. Experimental section

2.1. Materials

Novolac-type phenolic resin (PR) was kindly offered by the Institute of Chemistry, Chinese Academy of Sciences. *N*-Propanol was purchased from Guangzhou Chemical Reagent Factory, Guangzhou, China. HMTA, zirconium(IV) propoxide solution, acetylacetone, and triethoxymethylsilane were bought from Shanghai Aladdin Biochemical Technology Co., Ltd, Shanghai, China. All reagents without special mention were used as received.

2.2. Synthesis of preceramic polymer containing Zr/Si elements

Preceramic polymer containing Zr/Si elements (Zr/Si precursor) was synthesized according to previous work.[29,30] Briefly, zirconium propoxide and triethoxymethylsilane in a molar ratio of 5 : 4 were dissolved in *n*-propanol, and acetylacetone was used as the chelating agent. Deionized water was added to initiate the hydrolysis reaction of precursors. After 8 hours of reaction at 80 °C, the mixture was concentrated by distillation to deliver a light-yellow solution with a solid content of 35 wt%.

2.3. Preparation of PR-ZS hybrid aerogels

PR-ZS hybrid aerogels were prepared using a sol–gel method. First, PR (3 g) and HMTA (0.75 g) were dissolved in *n*-propanol (12 g) at room temperature by mechanical stirring. Then, various amounts of Zr/Si precursor were added dropwise into the above solution. The mixtures were transferred to sealed plastic vials and reacted at 80 °C for 2 days. The as-obtained wet gels were dried sequentially in a fume hood at room temperature for 1 day and in an air-circulating oven at 80 °C for 1 day. Subsequently, the dried aerogels were post-cured at 120 °C for 2 hours to enhance the crosslinking degree. Additionally, pure PR aerogels as the control samples were fabricated without addition of Zr/Si precursor in the same way. According to the added amount of solid Zr/Si precursor, the hybrid aerogels were referred to as PR-ZS10 (10 wt% of Zr/Si precursor in dried aerogels), PR-ZS20 (20 wt% of Zr/Si precursor in dried aerogels), PR-ZS30 (30 wt% of Zr/Si precursor in dried aerogels), and PR-ZS40 (40 wt% of Zr/Si precursor in dried aerogels).

2.4. Preparation of ZrC/SiC/C ceramic aerogels

To fabricate ZrC/SiC/C ceramic aerogels, the hybrid aerogels were pyrolyzed in a tube furnace at 1100 °C for 2 hours under an argon atmosphere with a heating rate of 2 °C min^{-1}, followed by heat treatment in a graphite furnace at 1700 °C for 2 hours under an argon atmosphere with a heating rate of 10 °C min^{-1}. These ceramic aerogels are designated as PR-ZS-1700. For comparison, pure carbon aerogels (PR-1700) were prepared from pure PR aerogels by the same procedure.

2.5. Characterization

The bulk density and linear shrinkage of aerogels were determined by measuring the dimensions and mass of cylindrical samples in the sequential processing steps.

The microstructure and elemental distribution of samples were investigated by scanning electron microscopy (SEM, JSM-7900F, JEOL, Japan) and transmission electron microscopy (TEM, JEM-2100F, JEOL, Japan). The molecular structure of Zr/Si precursor was characterized by Fourier transform infrared spectroscopy (FTIR, Nicolet iS5, Thermo Scientific, USA). The chemical structures of samples were investigated by X-ray photoelectron spectroscopy (XPS, Axis Supra+, Kratos, UK). X-ray diffraction (XRD) measurements were performed on a powder diffractometer (X'Pert PRO, PANalytical, Netherlands) using Cu/K_α radiation (40 kV, 40 mA, λ = 1.5418 Å). The specimens were continuously scanned from 5° to 90° (2θ) at a speed of 0.2° min^{-1}. N_2 adsorption–desorption isotherms were measured on a surface area and porosity analyzer (ASAP2460, Micromeritics, USA). Before measurements, the samples were degassed in vacuum at 100 °C for 12 hours. The Brunauer–Emmett–Teller (BET) method was utilized to calculate the specific surface areas (S_{BET}). The pore size distribution was estimated using the Barrett–Joyner–Halenda (BJH) model.

Thermogravimetric analysis (TGA, TGA/DSC 3+, METTLER TOLEDO, Switzerland) was carried out from room temperature to 900 °C at a heating rate of 10 °C min^{-1} in air and N_2 atmosphere. Compression tests were performed on cylindrical samples with the size of Φ 1.5 × H 2 cm using a universal test machine (68TM-30, Instron, USA) with a compression rate of 2 mm min^{-1}. Thermal conductivities were measured by the heat flux method (TPS 2500, Hot Disk AB, Sweden) at 25 °C. The specimens were cut and polished to ensure that top and bottom surfaces were smooth and parallel. The ablative and insulating behaviors were evaluated by a butane torch burning test for 300 s. Front and backside temperatures of the flat cylinder were recorded using an infrared thermometer and a thermocouple, respectively.

3. Results and discussion

3.1. Fabrication process and formation mechanism of aerogels

Fig. 1 illustrates the fabrication process and formation mechanism of PR-ZS hybrid aerogels and ZrC/SiC/C ceramic aerogels. Pure PR aerogels are prepared from PR solutions that contained PR, HMTA, and solvents. Under heating, HMTA catalyzes the crosslinking reaction of PR molecules, accompanied with phase separation between PR molecules and solvents, to generate an interconnected network structure. Through ambient pressure drying, the solvents in the interstices of PR are removed to generate pores, leading to the formation of PR aerogels.

The Zr/Si precursor solution (Fig. 2a) was synthesized from zirconium propoxide and triethoxymethylsilane. The presence of zirconium hydroxyl and silicon hydroxyl groups in Zr/Si precursor offers compatibility and potential chemical reaction sites with PR molecules. Fig. 2b illustrates the characteristic peaks of Zr/Si precursor in FT-IR spectra: Zr–O–C stretching vibration at 1530 cm^{-1},[31] CH_3–C═O stretching vibration at 1450 cm^{-1}, Si–CH_3 stretching vibration at 1260 cm^{-1}, Si–O–Si stretching vibration at 1020 cm^{-1},[32] Zr–O–Si absorption at 931 cm^{-1},[33] Si–OH stretching vibration at 854 cm^{-1},[34] Si–$(CH_3)_2$ absorption at 794 cm^{-1}, and Zr–OH stretching vibration at 610 cm^{-1}.[35] Thermal stability and pyrolysis behavior were assessed using TGA. As shown in Fig. 2c and d, Zr/Si precursor exhibits a small weight loss before 500 °C under both N_2 and air atmospheres due to solvent evaporation and decomposition of organic groups. Notably, the residual weight approaches 80% at 900 °C, indicating exceptional thermal stability.

After introduction of the Zr/Si precursor solution to original PR solution, a transparent solution with a light-orange color is exhibited (Fig. 2a), revealing the excellent compatibility between Zr/Si precursor and PR. Under the basic catalysis of HMTA, Zr/Si precursor molecules participate in the crosslinked network through chemical bonding with PR molecules. After the sol–gel reaction and ambient pressure drying, PR-ZS aerogels with intact appearance are obtained (Fig. 3a). Further, through the pyrolysis and carbonization processes, the hybrid aerogels are transformed into ZrC/SiC/C ceramic aerogels. The changes in linear shrinkage and apparent density of samples are presented in Table 1. As the Zr/Si precursor content increases, the linear shrinkage rate of the hybrid aerogels rises from 12.75% to 26.14%, and the apparent density increases from 0.31 g cm^{-3} to 0.65 g cm^{-3}. The introduction of Zr/Si precursor may interfere with the crosslinking reaction of PR molecules and affect the phase separation process, causing a larger shrinkage under capillary force. Also, the larger molar mass of Zr/Si elements than that of C is responsible for the increase of apparent density. During transformation from hybrid aerogels to ceramic aerogels, the carbothermal reduction reaction results in further increase of linear shrinkage and apparent density.

3.2. Microstructure and thermal stability of PR-ZS hybrid aerogels

SEM images show that PR and PR-ZS hybrid monolithic samples have the typical bicontinuous and percolating structures of aerogels that are generated by the sol–gel reaction.[14] The pore walls are composed of interconnected submicron aggregates which are stacked by primary nanoscale gel

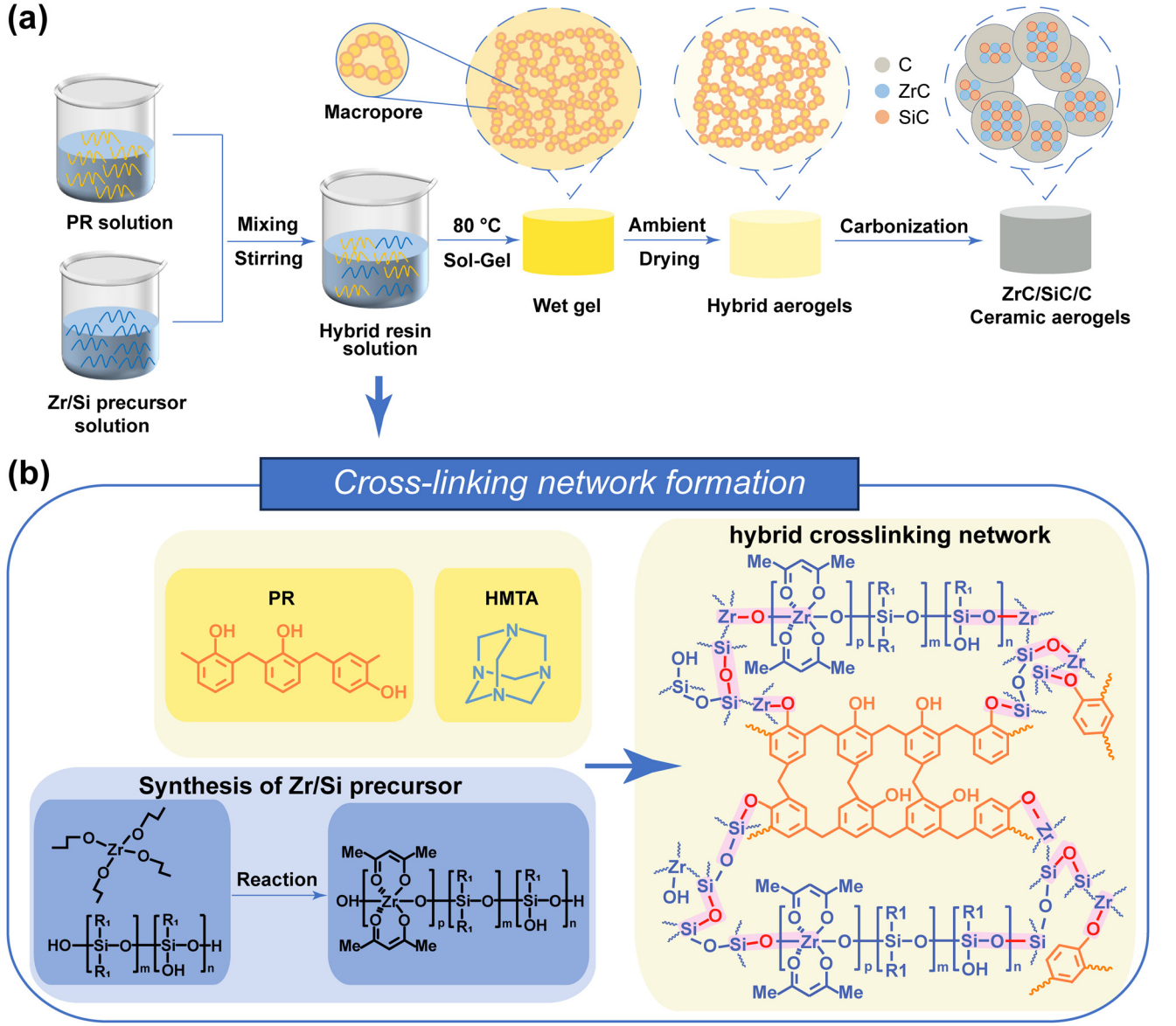

Fig. 1 Schematic of (a) the preparation process and (b) cross-linking network formation of aerogels.

particles. With the increase of the Zr/Si precursor content, the gel particle size gradually decreases from 184 nm in PR to 75 nm in PR-ZS40, and the pore size evidently reduces from 93 nm in PR to 50 nm in PR-ZS40. This is because Zr/Si precursor can interfere with the crosslinking reaction and phase separation process of PR by forming Zr–O–C and Si–O–C chemical bonds.

To study the porous properties of aerogels, N_2 adsorption measurements were conducted. As shown in Fig. 3c, the N_2 adsorption–desorption isotherms of all samples are consistent with typical type IV isotherms and H3 hysteresis loops at high relative pressure according to the IUPAC classification standard, indicating that these samples contain mesopores and macropores.[36] As the Zr/Si precursor content increases, the S_{BET} rises from 14.45 $m^2\ g^{-1}$ for PR to 89.53 $m^2\ g^{-1}$ for PR-ZS40 (Table 2). Concurrently, the mesoporous surface area (S_{Meso}) and mesoporous volume (V_{Meso}) gradually increase. The pore size distributions obtained from the desorption branch (insert in Fig. 3c) display broad peaks of a combination of mesopores and macropores, with the peak center shifting from 92 nm in PR to 49 nm in PR-ZS40. This behavior can be attributed to the introduction of Zr/Si precursor altering the crosslinked structure of PR, resulting in the formation of a denser network (Fig. 3b). The increased mesopores instead of macropores could more efficiently inhibit gas heat transfer and exert a positive effect on the thermal insulation performance of aerogels.

The thermal stability and oxidation resistance of PR and the hybrid aerogels were investigated by TGA (Fig. 4 and Table 3). In N_2 atmosphere (Fig. 4a and b), PR and PR-ZS aero-

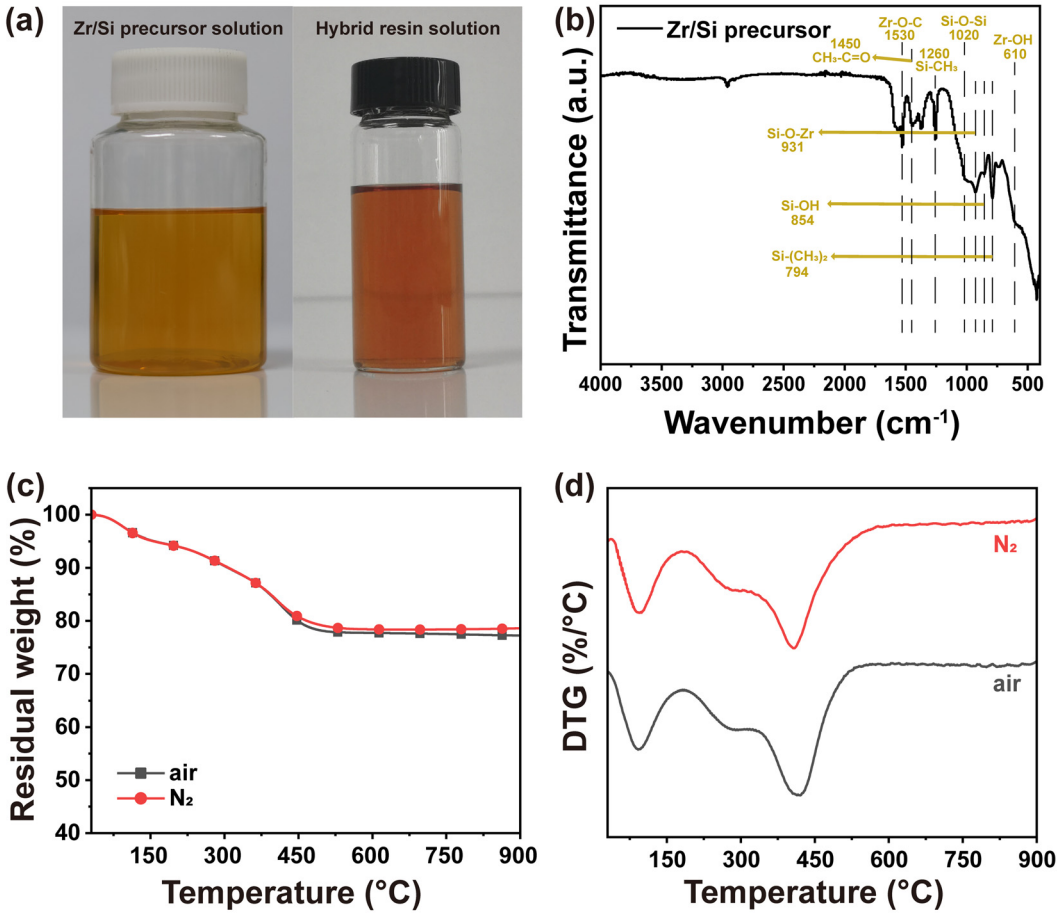

Fig. 2 (a) Digital photos of Zr/Si precursor solution and hybrid resin solution, (b) FTIR spectrum, (c) TGA and (d) DTG curves in air and N_2 atmosphere of Zr/Si precursor.

gels showed similar pyrolysis processes, and their thermal weight loss curves could be roughly divided into three stages. According to previous literatures,[34,37,38] the pyrolysis mechanism of PR aerogels is elucidated as follows. When the pyrolysis temperature is between room temperature and 240 °C, the weight loss is within 5% and is mainly due to the volatilization of solvents and water adsorbed by aerogels. At pyrolysis temperatures above 240 °C, the weight loss is due to the depolymerization of the PR matrix skeletal structure; the main pyrolysis products include CO, CO_2, and CH_4. The weight loss gradually becomes stable when the pyrolysis temperature exceeds 600 °C. The maximum decomposition rate (D_{Max}, the peak at temperature around 520 °C) of aerogels decreases with the increase of the Zr/Si precursor content. The residual weight at 900 °C (R_{900}) increases from 51.85% for PR to 61.05% for PR-ZS40. This is primarily due to the high bonding energy of the Zr–O and Si–O covalent bonds introduced by Zr/Si precursor which can effectively inhibit the decomposition of the hybrid aerogels.[39] On one hand, Zr/Si precursor reduces the number of phenolic hydroxyl groups, which are less thermally stable, by reacting with phenolic resin to generate Zr–O–C and Si–O–C bonds.[40] On the other hand, the Zr–O–Zr, Zr–O–Si, and Si–O–Si networks formed by the reaction between Zr/Si precursor can effectively enhance the overall thermal stability of aerogels. PR-ZS10 shows poor thermal stability, probably because the network structure of PR aerogels is destroyed by the addition of a small amount of Zr/Si precursor. In air atmosphere (Fig. 4c and d), the weight loss trend of aerogels with different Zr/Si precursor contents (Table 3) is similar to that in N_2 atmosphere. The R_{900} of PR aerogels is null. As the Zr/Si precursor content rises, the R_{900} increases. This is mainly attributed to the fact that silicon- and zirconium-containing functional groups in the hybrid aerogels are converted to silica and zirconia in the high-temperature oxidation environment.

3.3. Mechanical and thermal insulation properties of PR-ZS hybrid aerogels

The mechanical properties of aerogels play a crucial role in their practical use. Fig. 5a and b illustrate the compressive stress–strain behavior and compressive stress values of PR and PR-ZS aerogels. At relatively low densities (0.28–0.41 g cm^{-3}), these materials exhibit typical nonlinear deformation with the upward concavity compressive response of porous materials. The compressive curve shows a linear increase to a

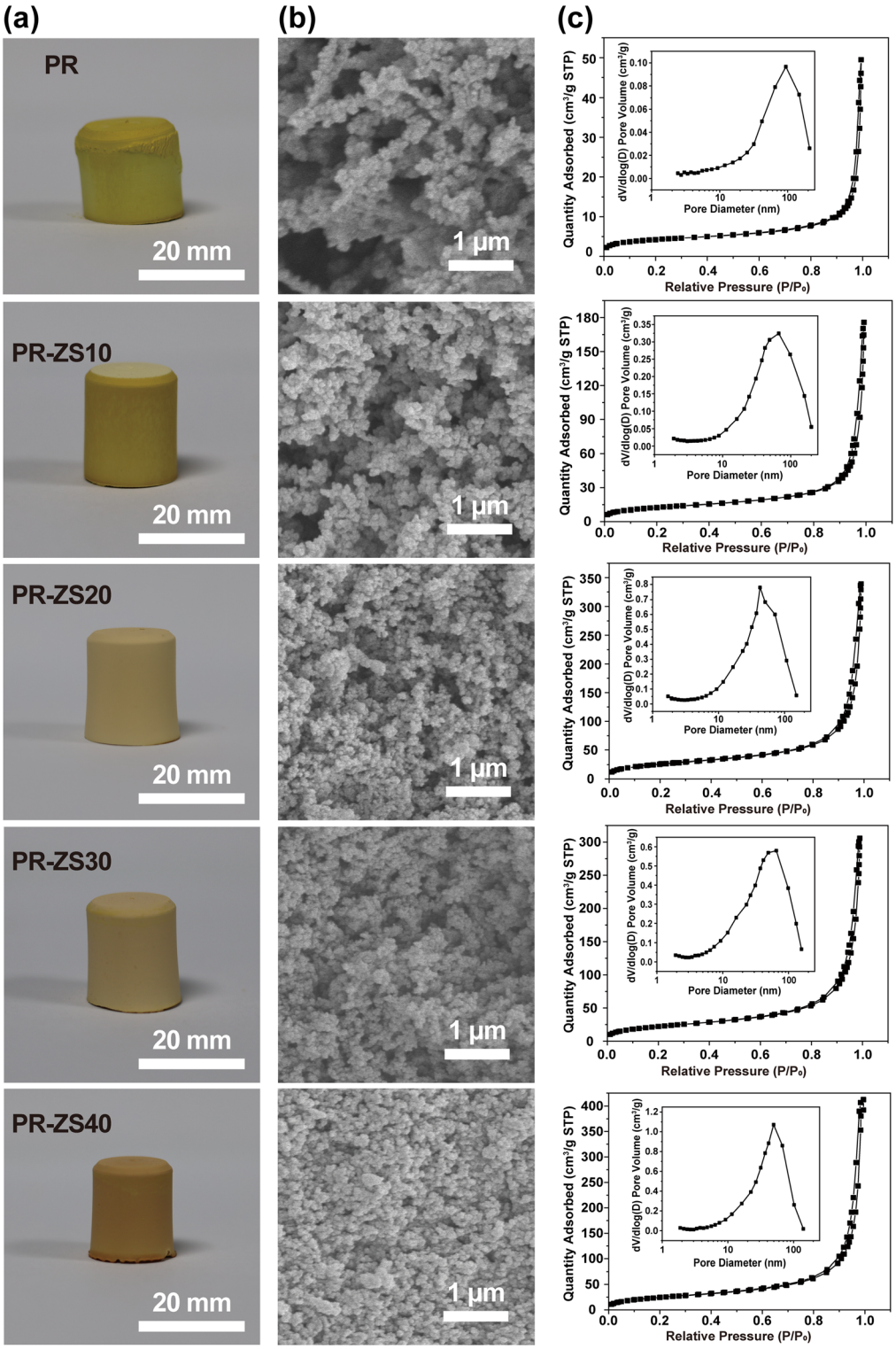

Fig. 3 (a) Digital photos, (b) SEM images, and (c) N_2 adsorption–desorption isotherms and BJH pore size distribution curves of PR and PR-ZS aerogels.

maximum elastic strain of approximately 5–7% (corresponding to compressive strength), then the slope dramatically decreases, after which the stress displays a rapid rise up to strains beyond 60%. The initial elastic stage is due to elastic bending or compression of the aerogel network, followed by irreversible yielding and densification stages accompanied by permanent damage.[41] For densities above 0.41 g cm^{-3}, the hybrid aerogels change from ductile to brittle, exhibiting

Table 1 Densities and linear shrinkages of aerogels

Sample	Density (g cm^{-3})	Linear shrinkage (%)
PR	0.28 ± 0.02	9.04
PR-ZS10	0.31 ± 0.03	12.75
PR-ZS20	0.41 ± 0.02	17.29
PR-ZS30	0.46 ± 0.04	19.25
PR-ZS40	0.65 ± 0.02	26.14
PR-1700	0.34 ± 0.04	27.44
PR-ZS20-1700	0.46 ± 0.01	26.76

Table 2 Textural characteristics of aerogels

Sample	S_{BET} (m^2 g^{-1})	S_{Meso} (m^2 g^{-1})	V_{Meso} (cm^3 g^{-1})	Porosity (%)
PR	14.45	8.76	0.07	76.90
PR-ZS10	44.27	31.52	0.27	73.24
PR-ZS20	91.76	76.35	0.52	64.72
PR-ZS30	80.77	69.97	0.47	65.21
PR-ZS40	89.53	87.21	0.63	53.25
PR-1700	18.62	12.59	0.16	74.01
PR-ZS20-1700	96.22	88.52	0.50	69.87

sudden failure at strains less than 13%. The higher compressibility of aerogels at lower densities is attributed to larger porosity, enabling bending deformation rather than fracture under compressive loads. The decrease in compressive strength of PR-ZS30 is probably caused by overdosed Zr/Si precursor altering the original crosslinking structure of PR and weakening the strength of the porous network.

The thermal insulation performance of aerogels was evaluated according to their thermal conductivity (Fig. 5d and Table 4). In general, the overall thermal conductivity comprises solid thermal conductivity (λ_s), gas thermal conductivity (λ_g), convection transmission conductivity (λ_c), and radiation transmission conductivity (λ_r),[42] as illustrated in Fig. 5c. Here, λ_c can be neglected because the pore size of the prepared aerogels is much smaller than the starting size of natural convection (>1 mm). Meanwhile, λ_r mainly plays a role in high temperature environments. Herein, the room temperature thermal conductivity of aerogels is mainly determined by λ_s and λ_g.[37,43] PR-ZS20 exhibits better thermal insulation features than the others and has the lowest thermal conductivity of 0.046 W (m K)$^{-1}$. This good performance can be attributed to the rich micro/nanopore structure and the low thermal conductivity of Zr–O and Si–O bonds as excellent phonon barriers, which greatly reduce the λ_s conduction.

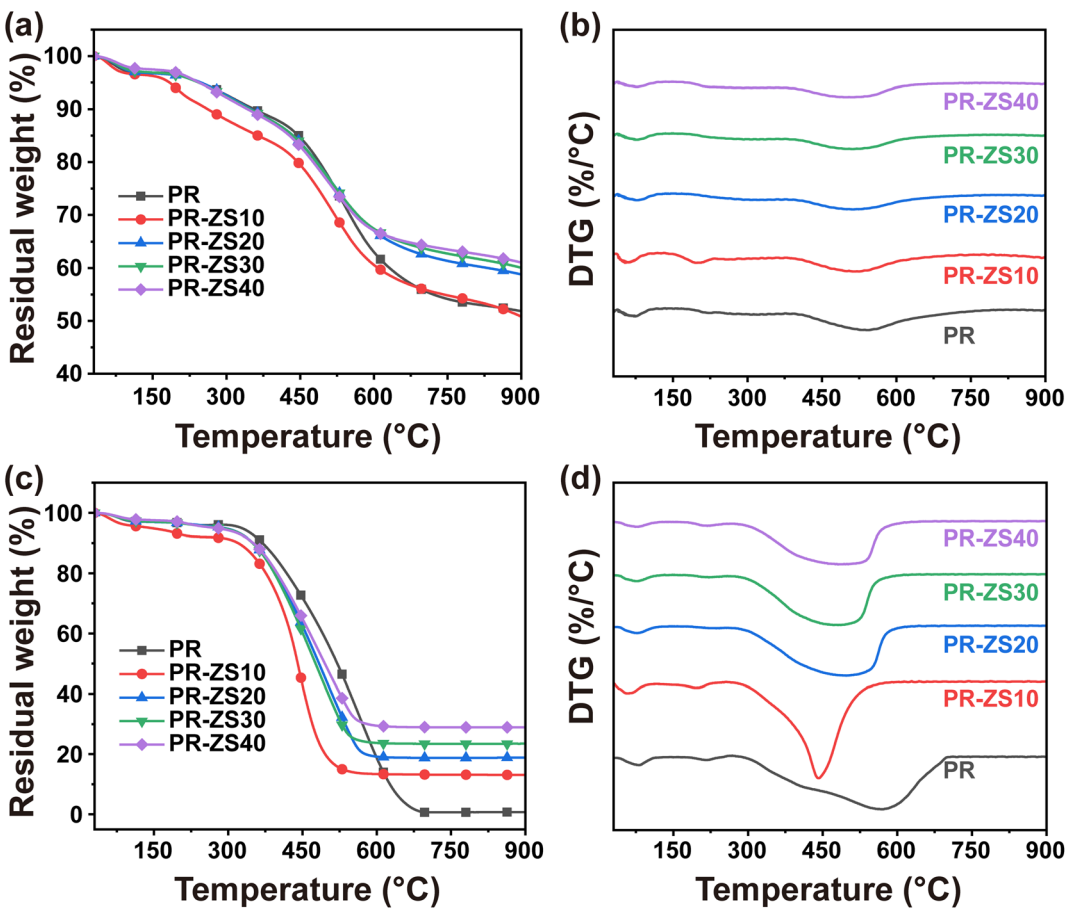

Fig. 4 TGA and DTG curves of PR and PR-ZS aerogels in (a and b) N_2 and (c and d) air atmospheres.

Table 3 TGA data of aerogels

Sample	$T_{d5\%}$ in air (°C)	$T_{d5\%}$ in N_2 (°C)	$T_{d10\%}$ in air (°C)	$T_{d10\%}$ in N_2 (°C)	R_{900} in air (%)	R_{900} in N_2 (%)
PR	326.17	247.17	369.33	356.17	0.73	51.85
PR-ZS10	141.83	184.17	320.17	261.83	13.11	50.81
PR-ZS20	290.17	248.00	350.17	349.67	18.81	58.80
PR-ZS30	284.50	243.50	349.33	347.33	23.46	60.06
PR-ZS40	271.67	244.50	350.67	343.00	28.90	61.05
PR-1700	655.00	—	668.00	—	3.72	—
PR-ZS20-1700	619.67	—	631.83	—	34.46	—

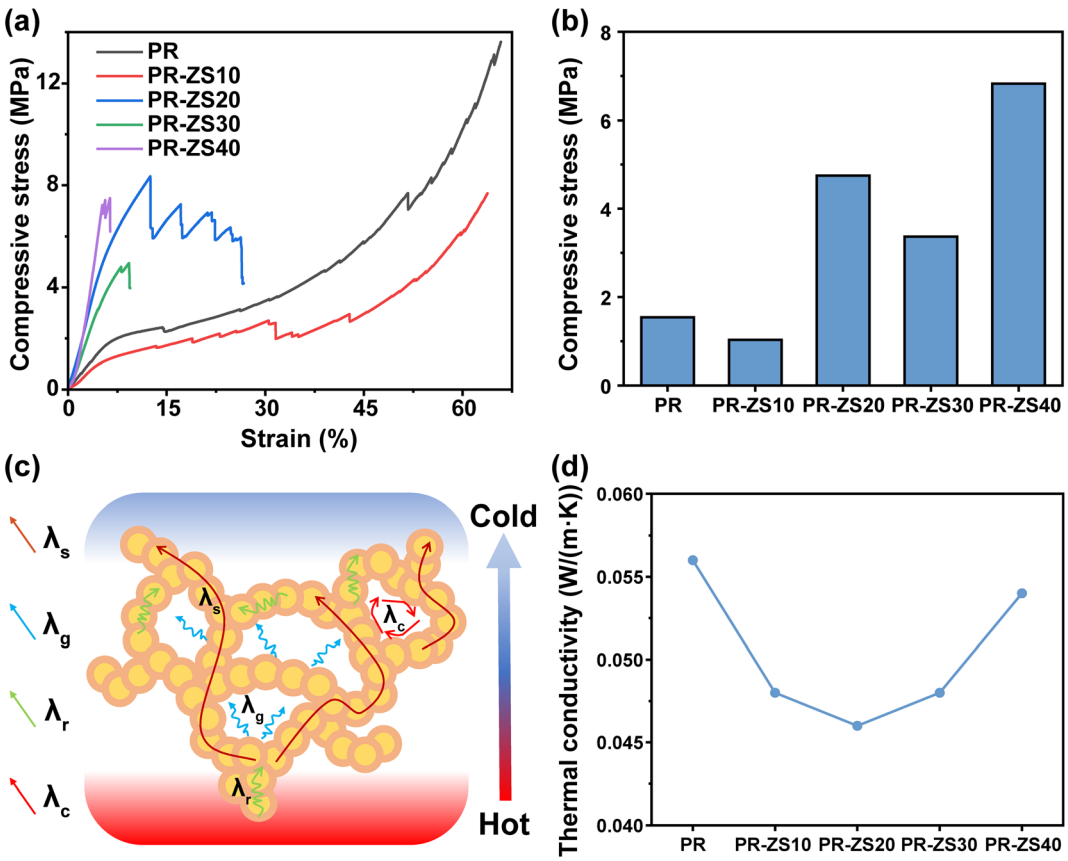

Fig. 5 (a) Compressive stress–strain curves, (b) compressive stress at 5% strain, (c) schematic of the heat insulation mechanism, and (d) room-temperature thermal conductivity of PR and PR-ZS aerogels.

Commonly, high mechanical strength and low thermal conductivity are considered mutually exclusive, and a balance between them is expected. In this study, the PR-ZS20 sample exhibits effective thermal insulation properties while maintaining high mechanical strength.

Table 4 Compressive stress and thermal conductivity data of aerogels

Sample	Density (g cm^{-3})	Compressive stress (MPa) at 5% strain	Thermal conductivity (W (m K)$^{-1}$)
PR	0.28 ± 0.02	1.54	0.056
PR-ZS10	0.31 ± 0.03	1.03	0.048
PR-ZS20	0.41 ± 0.02	4.75	0.046
PR-ZS30	0.46 ± 0.04	3.37	0.048
PR-ZS40	0.65 ± 0.02	6.83	0.054
PR-1700	0.34 ± 0.04	2.20	0.141
PR-ZS20-1700	0.46 ± 0.01	3.35	0.189

3.4. Structure and property investigation on ceramic aerogels

Based on the above analysis, PR-ZS20 was selected for high temperature carbonization to prepare ceramic aerogels, and the microstructure and properties of ceramic aerogels were studied. The microstructures of PR-ZS20 carbonized at different temperatures were observed by TEM images. As shown in Fig. 6a, PR-ZS20-1100 exhibits a typical aerogel network overlay structure, with amorphous SiO_2 and crystalline ZrO_2 nanoparticles surrounded by disordered carbon. In Fig. 6b, a crystal spacing of 0.30 nm corresponding to the ZrO_2 (0 1 1) plane can be evidently observed, but no diffraction fringe related to the SiO_2 crystal plane can be found,

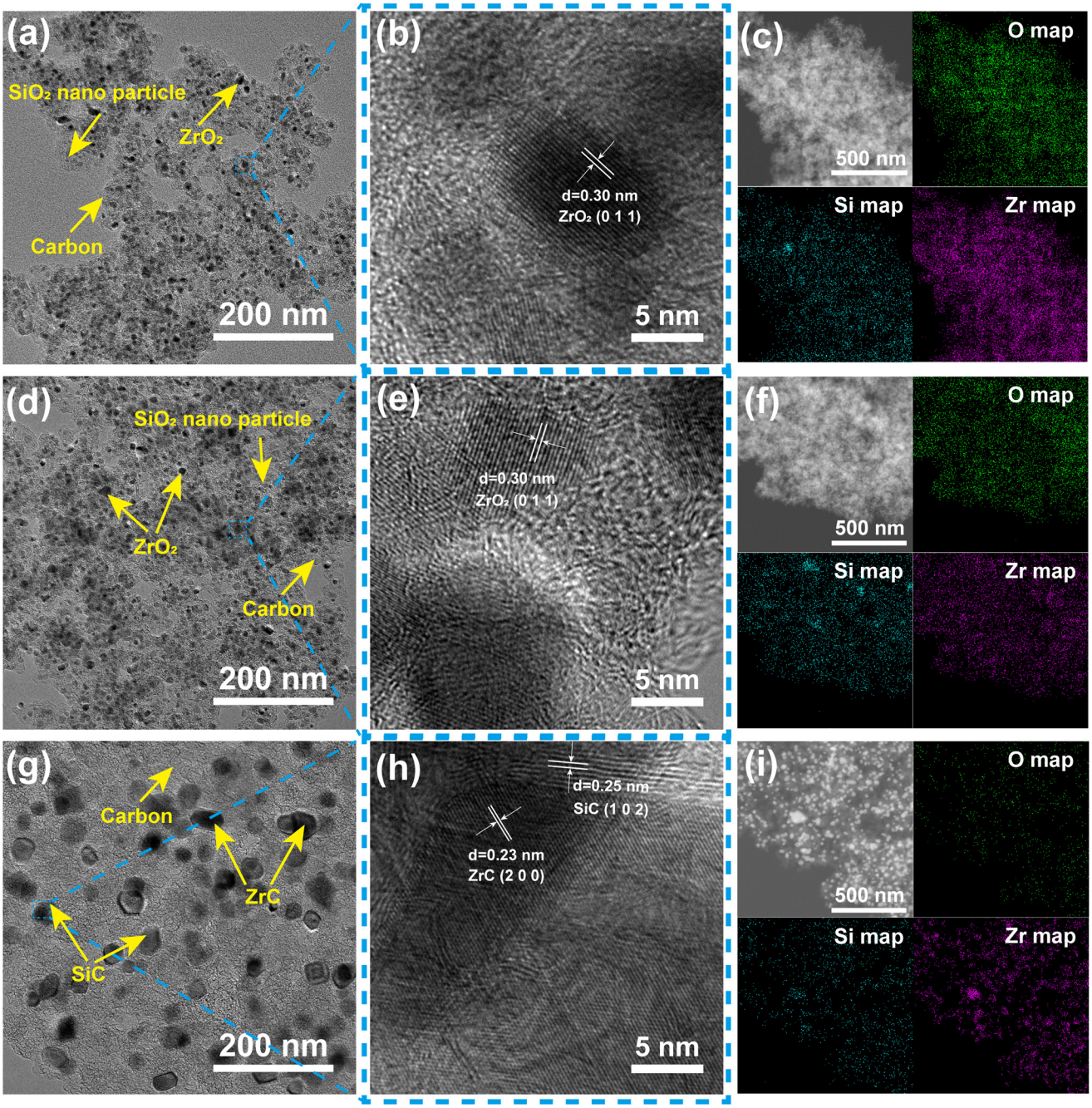

Fig. 6 TEM images, HRTEM images, and TEM mapping images of (a–c) PR-ZS20-1100, (d–f) PR-ZS20-1400, and (g–i) PR-ZS20-1700.

indicating that ZrO_2 exists in a crystalline state in the aerogel network, but SiO_2 and carbon are amorphous.[44] As the carbonization temperature rises to 1400 °C, ZrO_2 and SiO_2 nanoparticles begin to aggregate to form larger particles (Fig. 6d). In addition, there is still only a crystalline phase of ZrO_2 in Fig. 6e, indicating that SiO_2 is still amorphous. When the carbonization temperature reaches 1700 °C, the nanoparticles grow to 10–20 nm (Fig. 6g) with interplanar crystal spacings of 0.23 nm and 0.25 nm (Fig. 6h), which correspond to the ZrC (2 0 0) and SiC (1 0 2) planes, respectively.[45] Nanoparticles in PR-ZS20-1700 exhibit a relatively loose distribution due to growth of nanocrystals and consumption of carbon during the carbothermal reduction reaction. Moreover, it can be clearly seen that ZrC and SiC nanocrystals are adjacent to each other, leading to mutual inhibition of nanocrystal growth which contributes to their extraordinary dimensional stability at 1700 °C.

To further identify the structures of ceramic aerogels, XRD and XPS techniques were employed. Fig. 7a shows the XRD patterns of aerogel samples carbonized at 1100–1700 °C.

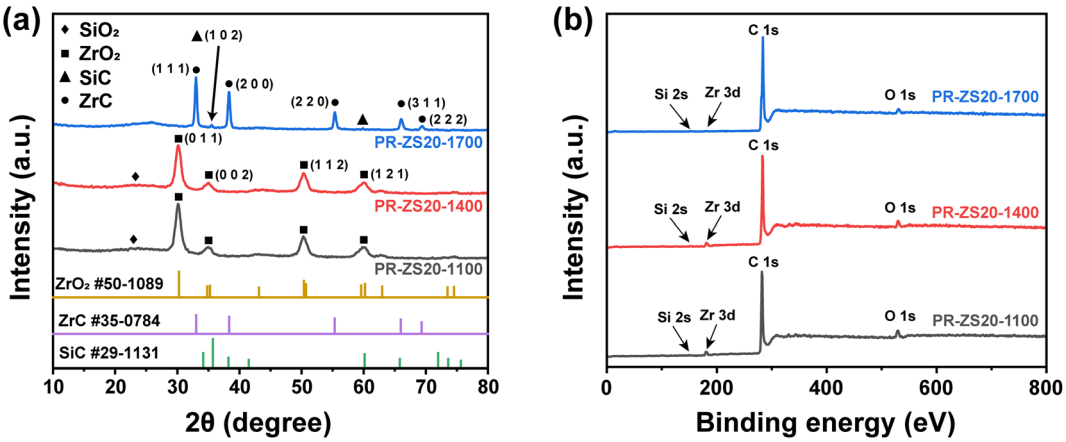

Fig. 7 (a) XRD patterns and (b) XPS spectra of PR-ZS20-1100, PR-ZS20-1400, and PR-ZS20-1700.

When the carbonization temperature is lower than 1400 °C, the diffraction peaks at 30.27°, 34.81°, 50.37°, and 60.20° assigned to the (0 1 1), (0 0 2), (1 1 2), and (1 2 1) planes of the ZrO_2 phase (PDF No. 50-1089) were clearly detected, confirming the existence of zirconia crystal phases. When the carbonization temperature reaches 1700 °C, the diffraction peaks at 35.73° and 60.15° assigned to the (1 0 2) and (1 1 0) planes of the SiC phase (PDF No. 29-1131) can be detected.[46] The diffraction peaks at 33.04°, 38.33°, 55.32°, 65.96°, and 69.30° assigned to the (1 1 1), (2 0 0), (2 2 0), (3 1 1), and (2 2 2) planes of the ZrC phase (PDF No. 35-0784) can be observed.[31] This confirms that the carbothermal reduction reaction occurs in PR-ZS20-1700, and crystalline SiC and ZrC are formed, which is consistent with TEM results. The XPS spectra show the presence of Si, Zr, C, and O peaks for all samples (Fig. 7b). With the increase of carbonization temperature, the element fraction of O decreases gradually, indicating that O atoms are consumed in the carbothermal reduction reaction.

The N_2 adsorption–desorption isotherms and BJH pore size distributions of PR-ZS20-1700 are shown in Fig. 8a. The N_2 adsorption–desorption isotherms of PR-ZS20-1700 exhibit a typical type IV isotherm, indicating the presence of mesopores

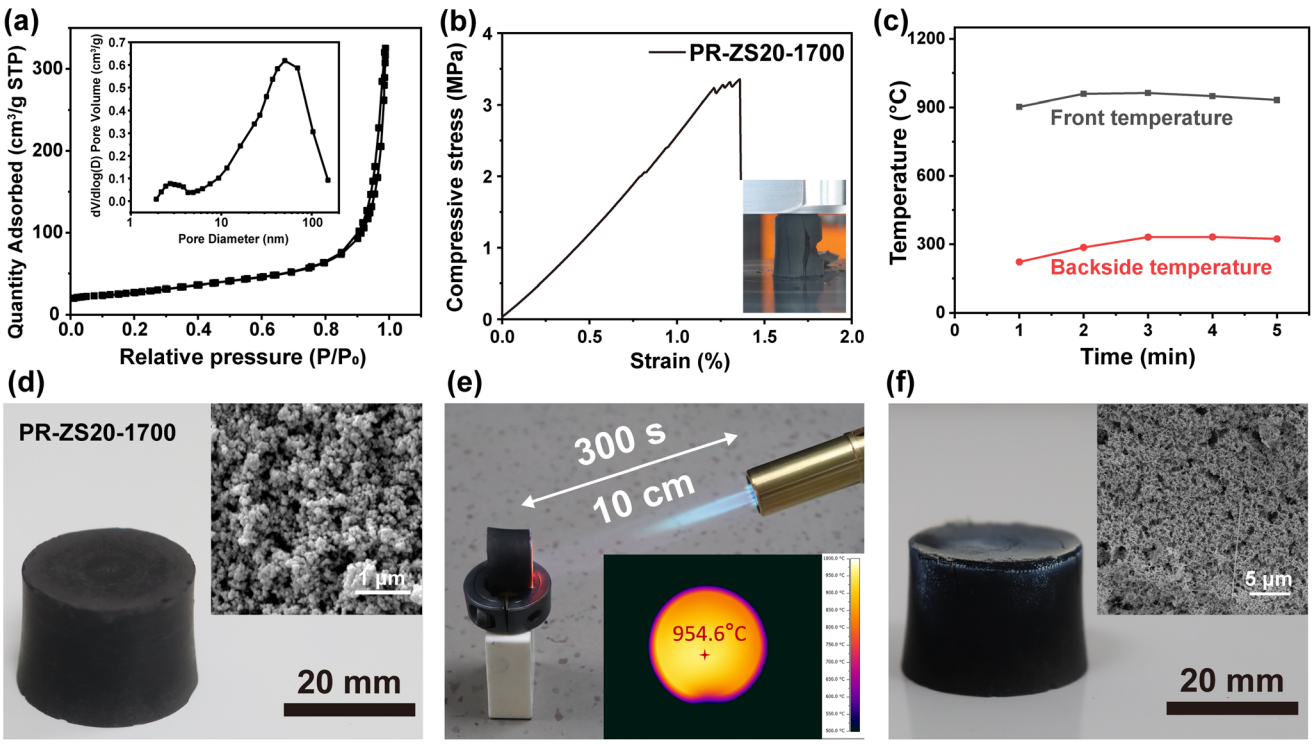

Fig. 8 (a) N_2 adsorption–desorption isotherms and BJH pore size distribution curve, (b) compressive stress–strain curve, and (c) front and backside temperatures during the ablation of PR-ZS20-1700. (d) Pristine sample, (e) sample during burning test, and (f) sample after burning test.

and macropores. S_{BET} increased from 91.76 m^2 g^{-1} for PR-ZS20 to 96.22 m^2 g^{-1} for PR-ZS20-1700 (Table 2) due to the formation of micropores during the pyrolysis and carbonization processes. The compressive stress–strain curve of PR-ZS20-1700 is illustrated in Fig. 8b. It can be seen that when the strain reaches 1.3%, the stress drops sharply, revealing the brittleness of ceramic aerogels (insert in Fig. 8b). Compared to PR-1700 (2.20 MPa), PR-ZS20-1700 demonstrates relatively high compressive strength (3.35 MPa) owing to the formation of silicon carbide and zirconium carbide nanoparticles (Table 4). Thermal stability in air atmosphere is a critical factor for assessing the reliability of aerogels. The R_{900} of PR-1700 in air atmosphere is 3.72%, while that of PR-ZS20-1700 is 34.46% (Table 3), proving the excellent oxidation resistance of ceramic aerogels.

The thermal ablative properties of the ZrC/SiC/C ceramic aerogels were evaluated under a dynamic ablative environment simulated by a butane torch burning test apparatus. When PR-ZS20-1700 is subjected to heat flow for 300 s, the front surface temperature rises to 960 °C, and the peak temperature of backside surface (20 mm from the front) is only about 330 °C (Fig. 8c). Fig. 8d–f show the appearance of PR-ZS20-1700 before, during, and after the butane torch burning test. Its shape remains unchanged with a white surface layer appearing due to the formation of oxide nanoparticles. In addition, the better ablative resistance performance of ceramic aerogels is demonstrated compared with that of carbon aerogels. The mass ablation rate of PR-ZS20-1700 is −0.0063 g min^{-1}, which is considerably lower than that of PR-1700 (0.056 g min^{-1}). Interestingly, the mass of the PR-ZS20-1700 sample increases rather than decreases after the burning test, which is caused by the oxidation of silicon carbide and zirconium carbide into silica and zirconia particles. Moreover, the oxide layer covering on the surface can protect the inner materials from the attack of oxygen.

4. Conclusions

In this work, hybrid phenolic aerogels were prepared by the sol–gel reaction of PR, Zr/Si precursor, and HMTA. Compared with pure phenolic aerogels, the hybrid aerogels have a similar interconnected porous structure but larger SSA, better thermo-oxidative stability, and higher compressive strength. The compressive stress of PR-ZS20 at 5% strain reaches 4.75 MPa while maintaining a low thermal conductivity (0.046 W $(m\ K)^{-1}$). After carbonization at 1700 °C, Zr/Si precursor is transformed into SiC and ZrC nanocrystals by the carbothermal reduction reaction, with the crystalline size around 10–20 nm. The ZrC/SiC/C ceramic aerogels demonstrate better ablative resistance and thermal insulation performance than the carbon aerogels derived from pure phenolic aerogels under the butane torch burning test. The linear ablation rate is as low as 0.017 mm min^{-1}, and the backside temperature at a depth of 20 mm is below 330 °C after 300 s of burning, while the front temperature is approximately 960 °C. These excellent properties prove that the hybrid aerogels and the ZrC/SiC/C ceramic aerogels are qualified candidates for thermal protection materials in long-term and high-temperature aerobic environments.

Author contributions

Ding Nie: writing – original draft, formal analysis, data curation. Hangyu Zhong: writing – original draft, formal analysis, data curation. Hongli Hu: formal analysis, data curation. Zhenhua Luo: writing – review & editing, resources, funding acquisition. Bo-xing Zhang: writing – review & editing, supervision, project administration, methodology, funding acquisition, conceptualization.

Data availability

The data supporting this article have been included as part of the ESI.†

Conflicts of interest

The authors have no conflicts of interest to declare.

References

1 S. S. Kistler, Coherent expanded aerogels and jellies, *Nature*, 1931, **127**, 741.
2 K. Wu, W. Dong, Y. Pan, J. Cao, Y. Zhang and D. Long, Lightweight and flexible phenolic aerogels with three-dimensional foam reinforcement for acoustic and thermal insulation, *Ind. Eng. Chem. Res.*, 2021, **60**, 1241–1249.
3 G. Zu, J. Shen, L. Zou, W. Wang, Y. Lian, Z. Zhang and A. Du, Nanoengineering super heat-resistant, strong alumina aerogels, *Chem. Mater.*, 2013, **25**, 4757–4764.
4 G. Zu, J. Shen, W. Wang, L. Zou, Y. Lian and Z. Zhang, Silica-titania composite aerogel photocatalysts by chemical liquid deposition of titania onto nanoporous silica scaffolds, *ACS Appl. Mater. Interfaces*, 2015, **7**, 5400–5409.
5 M. Zhou, Y. Tan, R. Chen, Y. Zhu, S. Cui, Q. Wang, L. Yu, C. Li and J. Zeng, Erythritol supported by carbon nanotubes reinforced alumina-silica aerogels as novel form-stable phase change materials with high photothermal conversion efficiency and greatly suppressed supercooling, *J. Energy Storage*, 2024, **90**, 111909.
6 J. Feng, C. Zhang, J. Feng, Y. Jiang and N. Zhao, Carbon aerogel composites prepared by ambient drying and using oxidized polyacrylonitrile fibers as reinforcements, *ACS Appl. Mater. Interfaces*, 2011, **3**, 4796–4803.
7 H. Tamon, H. Ishizaka, T. Araki and M. Okazaki, Control of mesoporous structure of organic and carbon aerogels, *Carbon*, 1998, **36**, 1257–1262.
8 H. Bi, Z. Yin, X. Cao, X. Xie, C. Tan, X. Huang, B. Chen, F. Chen, Q. Yang, X. Bu, X. Lu, L. Sun and H. Zhang,

Carbon fiber aerogel made from raw cotton: a novel, efficient and recyclable sorbent for oils and organic solvents, *Adv. Mater.*, 2013, **25**, 5916–5921.

9 Y. Badhe and B. Kandasubramanian, Reticulated three-dimensional network ablative composites for heat shields in thermal protection systems, *RSC Adv.*, 2014, **4**, 43708–43719.

10 H. Zhong, H. Hu, B. Ni, Y. Guo, Z. Luo, T. Zhao and B. Zhang, Silica sol nanoparticles hybridized allyl phenolic resins for improving mechanical and thermal performance, *Polymer*, 2022, **254**, 125052.

11 W. Song, X. Jia, C. Ma, J. Wang, W. Qiao and L. Ling, Facile fabrication of lightweight carbon fiber/phenolic ablator with improved flexibility via natural rubber modification, *Compos. Commun.*, 2022, **31**, 101119.

12 A. Harpale, S. Sawant, R. Kumar, D. Levin and H. B. Chew, Ablative thermal protection systems: pyrolysis modeling by scale-bridging molecular dynamics, *Carbon*, 2018, **130**, 315–324.

13 X. Jia, B. Dai, Z. Zhu, J. Wang, W. Qiao, D. Long and L. Ling, Strong and machinable carbon aerogel monoliths with low thermal conductivity prepared via ambient pressure drying, *Carbon*, 2016, **108**, 551–560.

14 S. Xu, J. Li, G. Qiao, H. Wang and T. Lu, Pore structure control of mesoporous carbon monoliths derived from mixtures of phenolic resin and ethylene glycol, *Carbon*, 2009, **47**, 2103–2111.

15 R. Yin, H. Cheng, C. Hong and X. Zhang, Synthesis and characterization of novel phenolic resin/silicone hybrid aerogel composites with enhanced thermal, mechanical and ablative properties, *Composites, Part A*, 2017, **101**, 500–510.

16 C. Wang, H. Cheng, C. Hong, X. Zhang and T. Zeng, Lightweight chopped carbon fibre reinforced silica-phenolic resin aerogel nanocomposite: facile preparation, properties and application to thermal protection, *Composites, Part A*, 2018, **112**, 81–90.

17 S. Ye, J. Feng and P. Wu, Highly elastic graphene oxide-epoxy composite aerogels via simple freeze-drying and subsequent routine curing, *J. Mater. Chem. A*, 2013, **1**, 3495–3502.

18 S. Yun, H. Luo and Y. Gao, Ambient-pressure drying synthesis of large resorcinol–formaldehyde-reinforced silica aerogels with enhanced mechanical strength and superhydrophobicity, *J. Mater. Chem. A*, 2014, **2**, 14542–14549.

19 S. Wang, H. Huang, Y. Tian and J. Huang, Effects of SiC content on mechanical, thermal and ablative properties of carbon/phenolic composites, *Ceram. Int.*, 2020, **46**, 16151–16156.

20 H. Huang, C. Hong, X. Jin, C. Wu, W. Wang, H. Wang, Y. Pan, S. Wu, X. Yan, W. Han and X. Zhang, Facile fabrication of superflexible and thermal insulating phenolic aerogels backboned by silicone networks, *Composites, Part A*, 2023, **164**, 107270.

21 P. Guo, J. Li, S. Pang, C. Hu, S. Tang and H. Cheng, Ultralight carbon fiber felt reinforced monolithic carbon aerogel composites with excellent thermal insulation performance, *Carbon*, 2021, **183**, 525–529.

22 Y. Hanzawa, H. Hatori, N. Yoshizawa and Y. Yamada, Structural changes in carbon aerogels with high temperature treatment, *Carbon*, 2002, **40**, 575–581.

23 H. Tamon, H. Ishizaka, M. Mikami and M. Okazaki, Porous structure of organic and carbon aerogels synthesized by sol-gel polycondensation of resorcinol with formaldehyde, *Carbon*, 1997, **35**, 791–796.

24 Z. Yang, J. Li, X. Xu, S. Pang, C. Hu, P. Guo, S. Tang and H. Cheng, Synthesis of monolithic carbon aerogels with high mechanical strength via ambient pressure drying without solvent exchange, *J. Mater. Sci. Technol.*, 2020, **50**, 66–74.

25 X. Li, J. Feng, Y. Jiang, L. Li and J. Feng, Anti-oxidation performance of carbon aerogel composites with SiCO ceramic inner coating, *Ceram. Int.*, 2019, **45**, 9704–9711.

26 K. Wu, Q. Zhou, J. Cao, Z. Qian, B. Niu and D. Long, Ultrahigh-strength carbon aerogels for high temperature thermal insulation, *J. Colloid Interface Sci.*, 2022, **609**, 667–675.

27 H. Liu, P. Wang, B. Zhang, H. Li, J. Li, Y. Li and Z. Chen, Enhanced thermal shrinkage behavior of phenolic-derived carbon aerogel-reinforced by HNTs with superior compressive strength performance, *Ceram. Int.*, 2021, **47**, 6487–6495.

28 P. Li, M. Shi, Z. Deng, P. Han, T. Yang, R. Hu, C. Dong, R. Wang and J. Ding, Achieving excellent oxidation resistance and mechanical properties of TiB_2-B_4C/carbon aerogel composites by quick-gelation and mechanical mixing, *Nanotechnol. Rev.*, 2022, **11**, 3031–3041.

29 W. Li, Y. Sun, L. Ye, W. Han, F. Chen, J. Zhang and T. Zhao, Preparation of high entropy nitride ceramic nanofibers from liquid precursor for CO_2 photocatalytic reduction, *J. Am. Ceram. Soc.*, 2022, **105**, 3729–3734.

30 C. Qin, H. Hu and B. Zhang, Monodispersed hollow ceramic microspheres fabricated based on preceramic polymers and pulse-controlled coaxial injection, *J. Am. Ceram. Soc.*, 2024, **107**, 5658–5667.

31 Z. Niu, B. Chen, S. Shen, H. Zhang, X. Ma, F. Chen, L. Li, Y. Xin, C. Zhang and X. Hou, Zirconium chelated hybrid phenolic resin with enhanced thermal and ablation resistance properties for thermal insulation composites, *Compos. Commun.*, 2022, **35**, 101284.

32 Q. Yuan, Y. Wang, Y. Huang, J. Tian, Z. Heng, M. Liang, Y. Chen and H. Zou, Nano co-continuous structure poly (imide-siloxane)/phenolic hybrid resin fabricated by copolymerization for the thermal protection system, *Ind. Eng. Chem. Res.*, 2023, **62**, 10477–10486.

33 H. Fu, Y. Qin, Z. Peng, J. Dou and Z. Huang, A novel co-continuous Si-Zr hybrid phenolic aerogel composite with excellent antioxidant ablation enabled by sea-island-like ceramic structure at high temperature, *Ceram. Int.*, 2024, **50**, 21008–21019.

34 Z. Niu, G. Li, X. Ma, S. Shen, Y. Xin, L. Cai, F. Chen, C. Zhang and X. Hou, Synergetic effect of O-POSS

and T-POSS to enhance ablative resistant of phenolic-based silica fiber composites via strong interphase strength and ceramic formation, *Composites, Part A*, 2022, **155**, 106855.

35 K. G. Severin, J. S. Ledford, B. A. Torgerson and K. A. Berglund, Characterization of titanium and zirconium valerate sol-gel films, *Chem. Mater.*, 1994, **6**, 890–898.

36 H. Cheng, C. Hong, X. Zhang, H. Xue, S. Meng and J. Han, Super flame-retardant lightweight rime-like carbon-phenolic nanofoam, *Sci. Rep.*, 2016, **6**, 33480.

37 Z. Niu, F. Qu, F. Chen, X. Ma, B. Chen, L. Wang, M. Xu, S. Wang, L. Jin, C. Zhang and X. Hou, Multifunctional integrated organic-inorganic-metal hybrid aerogel for excellent thermal insulation and electromagnetic shielding performance, *Nano-Micro Lett.*, 2024, **16**, 200.

38 Z. Niu, Y. Xin, L. Wang, S. Shen, X. Ma, B. Chen, C. Wang, F. Chen, C. Zhang and X. Hou, Two birds with one stone: construction of bifunctional-POSS hybridized boron-silicon ceramicized phenolic composites and its ablation behavior, *J. Mater. Sci. Technol.*, 2023, **141**, 199–208.

39 S. Li, Y. Han, F. Chen, Z. Luo, H. Li and T. Zhao, The effect of structure on thermal stability and anti-oxidation mechanism of silicone modified phenolic resin, *Polym. Degrad. Stab.*, 2016, **124**, 68–76.

40 H. He, L. Geng, F. Liu, B. Ma, W. Huang, L. Qu and B. Xu, Facile preparation of a phenolic aerogel with excellent flexibility for thermal insulation, *Eur. Polym. J.*, 2022, **163**, 110905.

41 H. Cheng, Z. Fan, C. Hong and X. Zhang, Lightweight multiscale hybrid carbon-quartz fiber fabric reinforced phenolic-silica aerogel nanocomposite for high temperature thermal protection, *Composites, Part A*, 2021, **143**, 106313.

42 G. Wang, J. Zhao, G. Wang, L. H. Mark, C. B. Park and G. Zhao, Low-density and structure-tunable microcellular PMMA foams with improved thermal-insulation and compressive mechanical properties, *Eur. Polym. J.*, 2017, **95**, 382–393.

43 X. Jin, C. Wu, H. Wang, Y. Pan, H. Huang, W. Wang, J. Fan, X. Yan, C. Hong and X. Zhang, Synergistic reinforcement and multiscaled design of lightweight heat protection and insulation integrated composite with outstanding high-temperature resistance up to 2500 °C, *Compos. Sci. Technol.*, 2023, **232**, 109878.

44 D. J. Smith, N. W. Jepps and T. F. Page, Observations of silicon carbide by high resolution transmission electron microscopy, *J. Microsc.*, 1978, **114**, 1–18.

45 X. Yao, S. Tan, Z. Huang, S. Dong and D. Jiang, Growth mechanism of β-SiC nanowires in SiC reticulated porous ceramics, *Ceram. Int.*, 2007, **33**, 901–904.

46 A. Zirakjou and M. Kokabi, SiC/C aerogels from biphenylene-bridged polysilsesquioxane/clay mineral nanocomposite aerogels, *Ceram. Int.*, 2020, **46**, 2194–2205.

